# Passive and active suppression of transduced noise in silicon spin qubits

Jaemin Park[1,3], Hyeongyu Jang[1,3], Hanseo Sohn [1], Jonginn Yun [1], Younguk Song [1], Byungwoo Kang[1], Lucas E. A. Stehouwer[2], Davide Degli Esposti[2], Giordano Scappucci [2] & Dohun Kim [1]✉

Addressing and mitigating decoherence sources plays an essential role in the development of a scalable quantum computing system, which requires low gate errors to be consistently maintained throughout the circuit execution. While nuclear spin-free materials, such as isotopically purified silicon, exhibit intrinsically promising coherence properties for electron spin qubits, the omnipresent charge noise, when converted to magnetic noise under a strong magnetic field gradient, often hinders stable qubit operation within a time frame comparable to the data acquisition time. Here, we demonstrate both open- and closed-loop suppression techniques for the transduced noise in silicon spin qubits, resulting in a more than two-fold (ten-fold) improvement of the inhomogeneous coherence time (Rabi oscillation quality) that leads to a single-qubit gate fidelity of over 99.6% even in the presence of a strong decoherence field gradient. Utilizing gate set tomography, we show that adaptive qubit control also reduces the non-Markovian noise in the system, which validates the stability of the gate fidelity. The technique can be used to learn multiple Hamiltonian parameters and is useful for the intermittent calibration of the circuit parameters with affordable experimental overhead, providing a useful subroutine during the repeated execution of general quantum circuits.

Spins in semiconductor quantum dots (QDs) offer a promising platform for developing large-scale quantum information processors[1–3]. Benefitting from isotopic purification, silicon spin qubits have recently enabled compelling demonstrations of coherent quantum operations of multiple qubits[4–7]. Single and two-qubit gate fidelities exceeding 99%[8–11] were realized along with elementary quantum error correction[12]. However, for fault-tolerant quantum computing, achieving consistent high-fidelity single- and two-qubit control is crucial, not only over an extended time but also across an extensive array of devices[13,14]. Therefore, the ability to precisely control the qubit parameters and a deeper understanding of the origin of the noise affecting the qubit system are pivotal steps toward developing mitigation strategies.

Real-time adaptive control, a powerful tool for stabilizing qubit operation via the active suppression of noise[15–19], allows the precise manipulation of quantum states. Experimental validations have been conducted, for example, in superconducting qubits[20,21], spins in diamond[22], and trapped atoms[23]. In the silicon QD platform, previous studies to address unwanted interactions between the spin qubits and the environment have focused on the automated correction of slowly drifting system parameters. These studies demonstrated, for example, reliable single- and two-qubit parameter calibration, including optimal readout points, using a field programmable gate array[7,24]. Although rapid progress has been made in optimizing the electrical controllability[25,26] while benefitting from intrinsically low magnetic noise sources, many of the silicon spin qubits fabricated thus far are

[1]Department of Physics and Astronomy, and Institute of Applied Physics, Seoul National University, Seoul, Korea. [2]QuTech and Kavli Institute of Nanoscience, Delft University of Technology, GA Delft, The Netherlands. [3]These authors contributed equally: Jaemin Park, Hyeongyu Jang. ✉e-mail: dohunkim@snu.ac.kr

negatively affected by transduced noise, which often extends to a wide range of frequencies. Dynamical decoupling methods such as spin-echo can extend the coherence time when the qubits are idle, but incorporating these complex pulse sequences with a general quantum algorithm is not straightforward. On the other hand, rapid estimation of the Hamiltonian parameter by Bayesian inference[27] has the potential for fast parameter calibration and is compatible with arbitrary qubit operations. Thus, the method can be used to improve the performance of qubits in a wide variety of quantum information processing applications.

Here, we demonstrate the rapid and real-time noise suppression in a $^{28}$Si/SiGe spin qubit device. We focus on both open- and closed-loop control on silicon spin qubits where the typical time scale of parameter fluctuation, due mainly to charge noise transduced to magnetic noise in the presence of a micromagnet, is comparable to the data acquisition time. For open-loop noise suppression, we investigate the controllable backaction of the charge sensor to the qubit where the rf-single electron transistor (rf-SET), referred to as a sensor dot (SD), close to the qubit acts as a noise source. In this case, the dynamic pulsing of the sensor chemical potential to the Coulomb blockade regime is used to suppress the noise in the qubit manipulation phase.

The remaining noise is additionally suppressed by a hardware-implemented Bayesian inference and frequency feedback circuit. By applying a methodology similar to that successfully demonstrated in GaAs devices[15–19], we confirm that fast parameter estimation and adaptive control can also boost the performance of qubits in $^{28}$Si/SiGe devices. The confirmed results reveal the general applicability of the active suppression technique based on Hamiltonian parameter estimation for both charge noise and nuclear spin noise suppression. Compared with the bare single-qubit gate fidelity of less than 98.6%, the technique enables single-qubit gate fidelity above 99.6% even in the presence of a large local magnetic field gradient and a significant source of charge noise. We further confirm the stability of the single-qubit gate performance using gate set tomography (GST) and discuss the potential of applying the method to fast two-qubit parameter estimation.

## Results

### The charge sensor-spin qubit system
We fabricated QD array devices with an overlapping gate layout[7,28] on an isotopically purified $^{28}$Si/SiGe heterostructure wafer (refer to the Methods section for fabrication details). The device is composed of an array of five gate-defined QDs and two SDs on both sides, as illustrated in Fig. 1a. We focus on the operation and measurement of the left SD and the leftmost qubit. On top of the device, we deposited a cobalt-based micromagnet of which the geometry is similar to that in previous studies[26]. Figure 1b shows the simulated magnetic field distribution near the qubit array, offset by an applied homogeneous magnetic field of 440 mT. In the line cut of the field profile, as shown in Fig. 1c, the measured qubit frequency is in good agreement with the simulation, revealing a strong spatial gradient $dB_z/dx = 0.184$ mT/nm at the location of the qubit. This enables each qubit to be individually and electrically addressed but simultaneously acts as a decoherence source.

Qubit manipulation involves applying a burst of microwaves to the upper screening gate $V_{screen}$ to induce electric dipole spin resonance. We use an energy-selective tunneling process near the charge transition of the last electron for qubit initialization and readout[29]. The SD is connected to an LC tank circuit for rf-reflectometry[30–32], which is performed by injecting a carrier signal at the frequency of 143 MHz and power of −100 dBm. The reflected power is monitored through cryogenic and room temperature amplification and subsequent homodyne detection with an integration time of 2 µs. See Supplementary Note. 1 for details of measurement setup.

### Passive noise suppression
We first demonstrate passive suppression of the transduced noise. Figure 2a illustrates the qubit capacitively coupled to SD. The back-action of the SD on the qubit[33,34] is marked by arrows in Fig. 2a, which arises from electron transport through the Coulomb blockade-lifted SD, whose fluctuations lead to that of the position of the qubit. This type of noise was commonly investigated by detecting the discrete fluctuations in the transport current[31], but here we investigate its effect on the qubit coherence. Although it is commonly believed that this
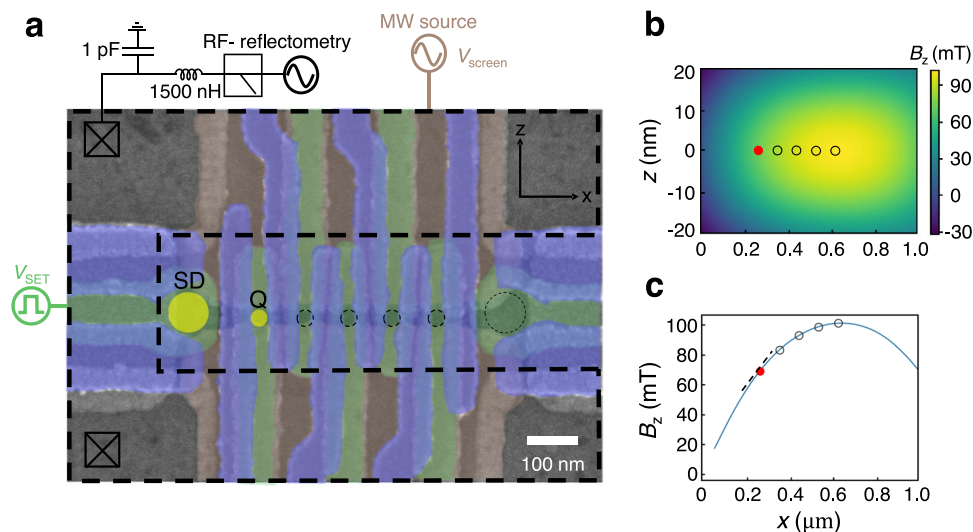


**Fig. 1 | Linear array $^{28}$Si/SiGe quantum dot (QD) device. a** False-colored scanning electron microscopy image of the device before the deposition of the micromagnet. Three overlapping gate layers were fabricated on an isotopically purified $^{28}$Si/SiGe heterostructure. The first (brown), second (green), and third (purple) layers contain screening gates, plunger gates, and barrier gates for the qubit array and sensor dots, respectively. The QDs not used for the current experiment are indicated by dotted circles. The shape of the micromagnet is depicted by a bold dashed line. **b** Numerical field distribution near the qubit area produced by the micromagnet. Circles indicate the expected locations of QDs. **c** Field profile along the qubit array axis (z = 0 nm). Circles indicate measured qubit resonance frequencies while the solid curve is numerically simulated. The black dashed line represents the gradient of $B_z$, $dB_z/dx = 0.184$ mT/nm at the location of the qubit. In (**b, c**), the magnetic field values are offset by the externally applied $B_z = 440$ mT.
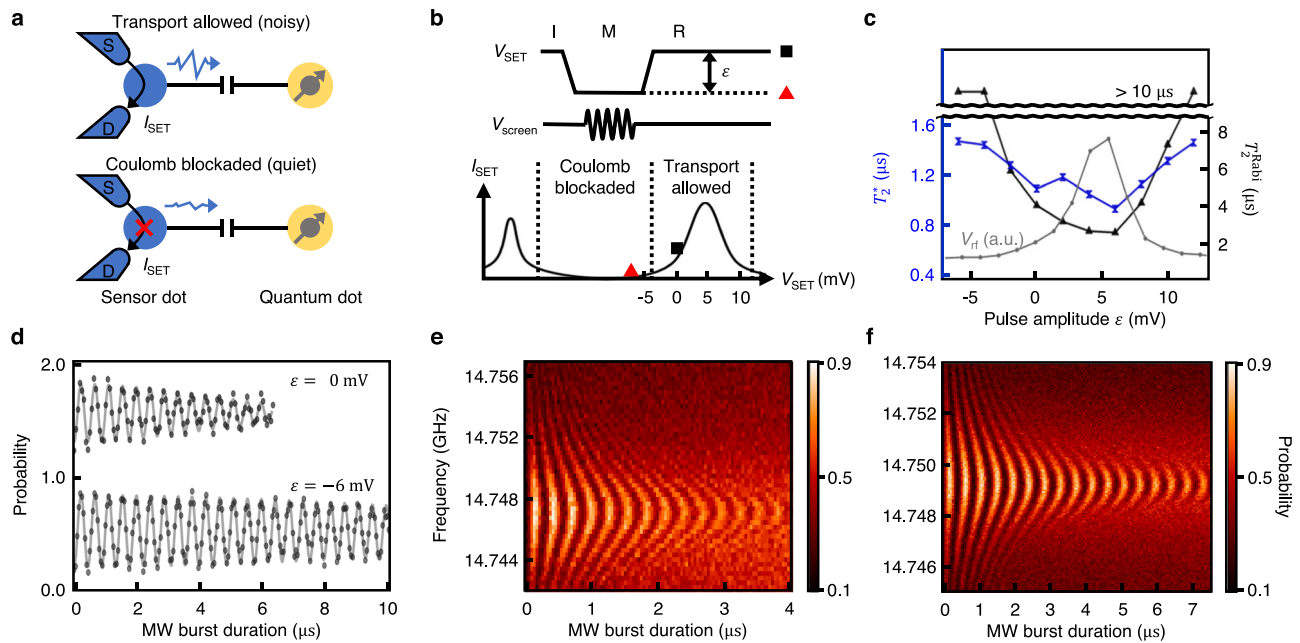
**Fig. 2 | Passive suppression of transduced noise. a** Schematic diagram of the proximal charge sensor and qubit where the sensor dot (SD) is tunnel-coupled to the source and drain, and capacitively coupled to the qubit dot. Top: In the transport-allowed regime, the charge sensor is active and sensitive to the change of charge number in the qubit, but its backaction to the qubit is also enhanced. Bottom: The charge sensor in the Coulomb blockade regime disturbs the qubit minimally. **b** Sequence for dynamic pulsing of SD chemical potential. The SD plunger gate voltage $V_{SET}$ is set at the maximally sensitive point (bottom plot, black box) during the qubit initialization (I) and readout (R). For qubit manipulation (M), $V_{SET}$ is pulsed to the Coulomb blockaded regime (bottom plot, red triangle). **c** Inhomogeneous coherence time $T_2^*$ (blue) and Rabi decay time $T_2^{Rabi}$ (black) with varying dynamic pulsing voltage $\varepsilon$. The rf-reflectometry signal proportional to the transport current $I_{SET}$ is plotted in gray. The data acquisition time for each point is 5 min. **d** Comparison of Rabi oscillations with and without dynamic pulsing of SD. The two oscillating probabilities are offset by 1.0 for clarity. Rabi chevron patterns when $\varepsilon = 0$ mV (**e**) and $\varepsilon = -6$ mV (**f**).

backaction can be lowered by turning off the carrier power for the qubit manipulation phase[35,36], we note that significant qubit dephasing still occurs as long as electron transport is allowed in the SD (see Supplementary Note. 2 for details of sensor-qubit coupling). Thus, the main way to suppress the noise is to dynamically pulse the plunger gate of the SD, $V_{SET}$, by the amount of $\varepsilon$ towards the Coulomb blockaded regime during qubit manipulation, as schematically shown in Fig. 2b. For the qubit measurement, $V_{SET}$ is pulsed back to the regime in which the sensor is maximally sensitive to changes in the charge number in the nearby QD.

Figure 2c shows the variation in the inhomogeneous coherence time $T_2^*$, measured by Ramsey interference measurement, and Rabi decay time $T_2^{Rabi}$ as functions of $\varepsilon$. Starting from the minimum $T_2^*$ ($T_2^{Rabi}$) of about 0.92 (2.52) μs when maximum transport current is allowed through SD ($\varepsilon = 6$ mV), the qubit demonstrates improved coherence as the chemical potential of SD is pulsed towards the Coulomb blockade regime, and the behavior is expected to be periodic per that of the Coulomb oscillations in SD. For $\varepsilon = -6$ mV, we observe an increase in $T_2^*$ ($T_2^{Rabi}$) of more than 75% (500%) compared with the case of $\varepsilon = 0$ mV. Consequently, as shown in Fig. 2d, the Rabi oscillation quality under resonant conditions is significantly increased, thereby attesting to the effectiveness of the dynamic pulsing of the SD chemical potential. Moreover, taking into account frequency detuning, a comparison of the Rabi chevron pattern between the case of $\varepsilon = 0$ mV (Fig. 2e) and $\varepsilon = -6$ mV (Fig. 2f) also shows that the qubit driving quality is directly enhanced, as Fig. 2f exhibits improved clarity and contrast in probability oscillations. The resonant frequency shift in Fig. 2f, which corresponds to pulsing by $\varepsilon = -6$ mV, using the field distribution determined in Fig. 1c, translates to a position shift of the qubit by about 0.33 nm, which is unlikely to lead to significantly different distributions of the nuclear spins in the host material. Therefore, the decoherence is primarily attributed to the charge noise transduced to magnetic noise.

## Noise spectroscopy

Fluctuations in the qubit frequency were observed in both the time and frequency domains through repeated Ramsey experiments for $\varepsilon = 0$ and $-6$ mV, as shown in Fig. 3a, b. Comparing Fig. 3a, b, we note that slow frequency fluctuation remains even after the application of passive noise suppression. Although suppressing the noise originating from the SD notably enhanced $T_2^*$ and $T_2^{Rabi}$, the effect is not apparent in the repeated Ramsey experiment, due to the limited frequency sampling rate in this case of 0.548 Sa/s.

To enhance the frequency estimation rate, we employed Bayesian inference of the qubit frequency based on one hundred single-shot outcomes of the Ramsey experiment where the free evolution time increased from 40 ns to 4 μs in steps of 40 ns (refer to the Methods section for details). Consequently, the estimation cycle takes 24 ms (100 × 240 μs), where one shot of measurements consists of a microwave burst and waiting time of 60 μs for reducing the heating effect[7,37], a readout duration of 140 μs, and a calculation time of 40 μs for Bayesian inference.

Figure 3c shows the variance of the frequency fluctuation $\sigma^2 = 2D_\alpha T^\alpha$ as a function of time interval $T$ where $D_\alpha$ is the diffusion coefficient. We note that $\sigma^2$ follows sub-diffusive behavior[38] with an exponent $\alpha = 0.58$ (0.47) and $D_\alpha = 0.0179$ MHz$^2$/s$^{0.58}$ (0.0119 MHz$^2$/s$^{0.47}$) for $\varepsilon = 0$ mV ($-6$ mV). The reduction of $\alpha$ and $D_\alpha$ suggests the suppression of noise stemming from the SD backaction over $T$. Using 30,000 samples obtained from the Bayesian inference, we also observe that dynamically pulsing SD results in an overall reduction in the noise power spectral density PSD, as shown in Fig. 3d. We fit the PSD to power-law spectra $A/f^\beta$ with a noise amplitude $A = 0.00296$ MHz$^2$/Hz (0.00175 MHz$^2$/Hz) and an exponent $\beta = 1.34$ (1.17) for $\varepsilon = 0$ mV ($-6$ mV). Thus, we confirm that, as the sensor backaction is suppressed by dynamic pulsing, so is the noise amplitude of fluctuations in the qubit frequency.
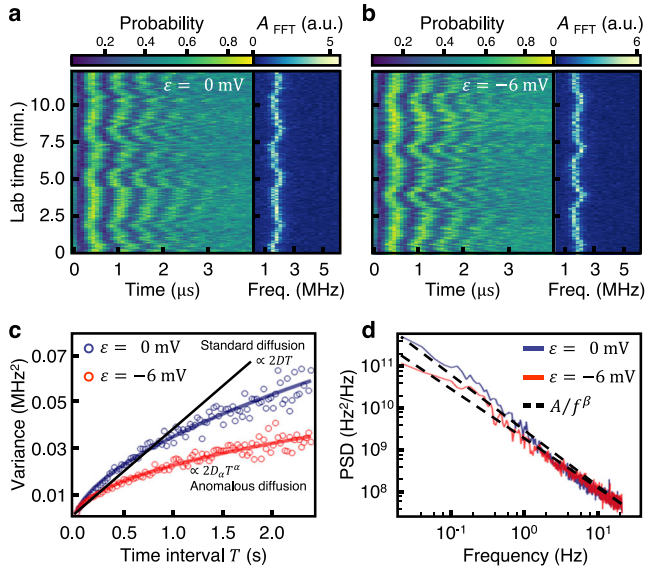
**Fig. 3 | Noise spectroscopy.** Repeated Ramsey interference as a function of the free evolution time with a fixed off-resonance microwave frequency for $\varepsilon = 0$ mV (**a**) and $\varepsilon = -6$ mV (**b**). Panels on the right in (**a**, **b**): Fast Fourier transform (FFT) of the time domain data. **c** Variance of the resonance frequency fluctuation as functions of the time interval $T$. The solid curves are fit to functions of the form $2D_\alpha T^\alpha$ where $D_\alpha$ is a diffusion coefficient. The linear line is overlaid as an example of standard diffusion, i.e., Brownian motion. **d** The power spectral density PSD of the noise determined by Bayesian inference. The dashed lines are fit to the power-law decay of the form $A / f^\beta$.

To further analyze the PSD, we focus on the decay envelope of Ramsey oscillation with the free evolution time $t$, as represented by the decoherence function (see Supplementary Note. 3 for details of derivation)[39,40]

$$W(t) = \exp\left(-t^2 / \left(T_2^*\right)^2\right) = \exp\left(-\frac{t^2}{2}(2\pi)^2 \int_{f_0}^{\infty} df\, S(f)\, \mathrm{sinc}^2(\pi f t)\right)$$
(1)

where $f_0$ is the reciprocal of the total integration time of the experiment (~5 min) and $S(f)$ is the PSD. Substituting the fitting parameters $A$ and $\beta$ in $S(f)$, the integral yields theoretical $T_2^*$ of 0.916 μs for $\varepsilon = 0$ mV and 1.404 μs for $\varepsilon = -6$ mV, which are in good agreement with the experimentally measured values (Fig. 2c) within the uncertainty of the fitting procedures. Moreover, one can obtain the quasi-static variance $\sigma_{static} = 1 / \sqrt{2\pi} T_2^*$ from Eq. (1) of 245.69 kHz (160.28 kHz) for $\varepsilon = 0$ mV (−6 mV). $\Delta\sigma_{static}$ of 85.41 kHz reflects the reduced noise achieved by dynamic SD pulsing while residual noise 160.28 kHz may stem from other transduced noise sources distributed in the system that are not properly controlled.

**Active noise suppression**
Applying the passive noise suppression technique by default, we further implemented active feedback control to suppress the remaining noise. We used the Bayesian inference described above as a probing tool and separated the experimental sequence into probe and operation steps, as illustrated in Fig. 4a. To collect 100 single-shot outcomes during the probe phase, π/2 rotation pulses separated by varying free evolution time were applied, where the frequencies $f_{MW}$ are detuned by 2 MHz from the local oscillator frequency. We then calculated the instantaneous estimation of the frequency $f_{est}$ and the frequency error $\Delta f$ between the target frequency $f_{target}$ and $f_{est}$. Subsequently, the microwave frequency $f_{MW}$ was adaptively adjusted by $\Delta f$ in the operation step.

Figure 4b demonstrates the stabilization of the qubit frequency during the operation phase by successfully locking it to $f_{target} = 2$ MHz. The inset in Fig. 4b displays a histogram of qubit frequencies with (red) and without (blue) adaptive control. As $f_{MW}$ is adaptively corrected, the histogram exhibits a narrow distribution with a frequency uncertainty of 65.3 kHz, reflecting a decrease in deviation of 40.7% in comparison with $\sigma_{static} = 160.28$ kHz that was obtained from the noise spectrum. Furthermore, as shown in Fig. 4c, the noise amplitude of PSD decreases from 1553 to 837 kHz²/Hz, indicating the suppression of residual noise. The flattened low-frequency noise of about $2.5 \times 10^{10}$ Hz²/Hz below the bandwidth of 0.1 Hz is indicative of successful noise filtering by active feedback control.

The stabilized qubit operation is also evident from the repeated Ramsey experiment with active frequency feedback, as shown in Fig. 4d. As shown in Fig. 4e, the Ramsey oscillations with active feedback reveal a more than 2-fold improvement in $T_2^*$ of 3.21 μs. This improvement corresponds to a deviation of 70.11 kHz estimated from $\sigma_{static} = 1 / \sqrt{2}\pi T_2^*$, which is also close to the frequency uncertainty in the histogram in Fig. 4b. The fitted red solid line in Fig. 4e also yields an oscillation frequency of 1.93 MHz, in excellent agreement with the target frequency of 2 MHz within the uncertainty of the frequency estimation of 70.11 kHz.

As an example of the compatibility of the method with general operation sequences, we perform a Rabi chevron experiment with controlled detuning by adaptive control. Figure 4f shows a clear improvement of oscillation quality and contrast in probability oscillation compared with that of non-adaptive control (Fig. 2f). Different from the passive suppression technique, active feedback control enables effective noise suppression without requiring precise knowledge of the noise origin. This universality has been demonstrated across the various platforms for quantum information processing, as discussed in the introduction above, and implies scalability towards multi-qubit correction. In Supplementary Note 4. we present preliminary data showing qubit frequency estimation when strong exchange interaction is present in the two-qubit system, which further shows the possibility of applying the developed method to correct multiple Hamiltonian parameters[41,42].

**Gate set tomography**
We turn to confirm the improved stability of the qubit operation enabled by adaptive control using GST[43,44], which allows the detection of specific errors for each circuit. We perform a single-qubit GST combined with frequency feedback of which schematic pulse sequence is shown in Fig. 5a. This combined GST protocol extends the total experiment time to over 6 h, allowing a thorough assessment of the robustness of the entire system. The density matrix showing initialization and measurement fidelity (top row) and the Pauli transfer matrix for gates X/2 and Y/2 (bottom row) are shown in Fig. 5b, c for GST without (with) applying passive and active noise suppression techniques. The initialization and measurement fidelity remain unchanged, indicating that the developed methods do not address state preparation and measurement (SPAM) errors. Instead, these techniques enhance the gate fidelities, $F_{X/2}$ from 98.56% to 99.66% and $F_{Y/2}$ from 98.57% to 99.49%, showing the improved stability of the qubit system.

The GST protocol is based on a Markovian gate set, assuming stationary noises for error prediction. Consequently, the GST model fails to accurately fit data influenced by non-Markovian noise the degree of which can be evaluated by the goodness-of-fit[43,44]. The method determines that the noise is sufficiently Markovian if the following inequality is satisfied.

$$k - \sqrt{2k} < 2\Delta \log L_s < k + \sqrt{2k}$$
(2)

where $\log L_s$ is the log-likelihood ratio between the predicted and observed probability and $2\Delta \log L_s = 2 \log L_{max,s} - 2 \log L_s$ is

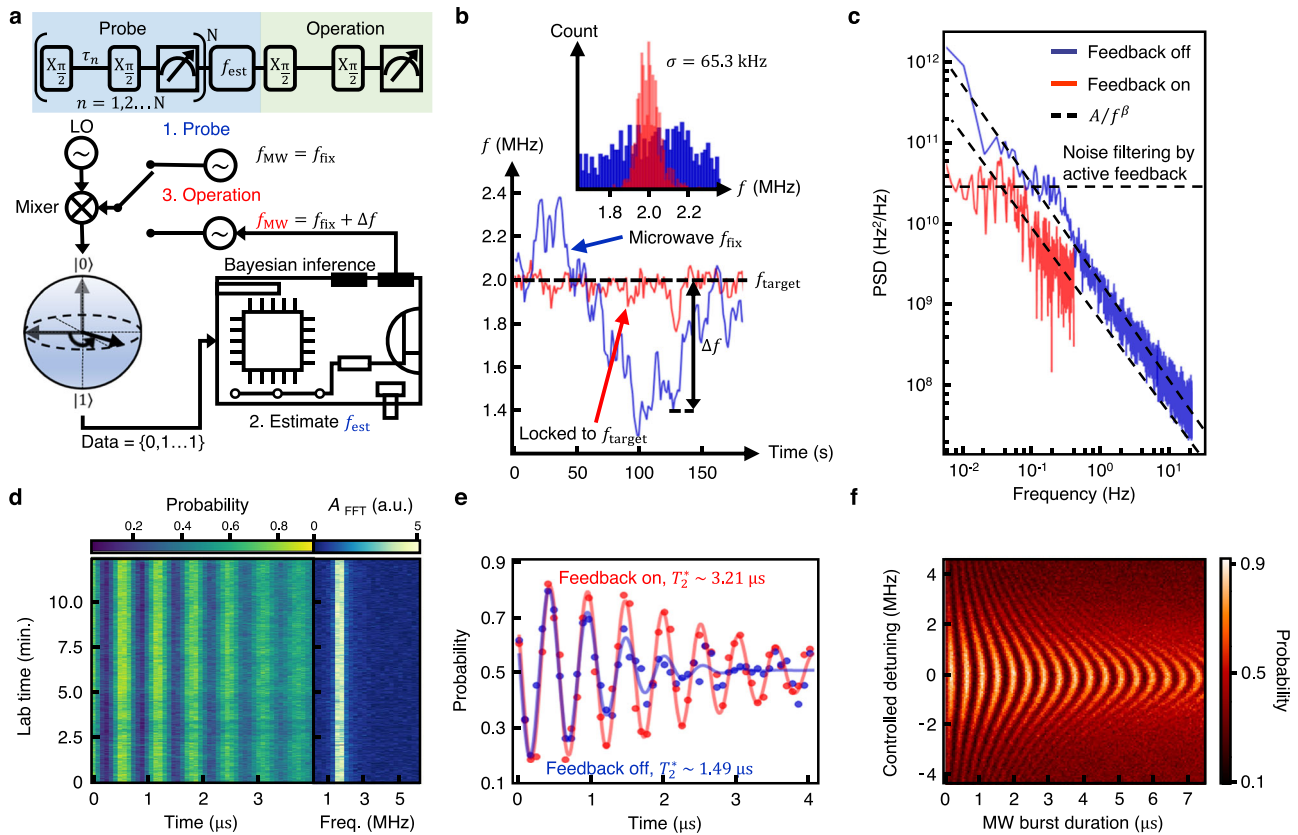**Fig. 4 | Active feedback control. a** Top: Experimental sequence of feedback control. N single-shot outcomes are collected in the probe phase, followed by estimation of the qubit frequency $f_{est}$ by the Bayesian inference circuit. The adaptive correction of the microwave frequency $f_{MW}$ is performed for the qubit operation in the next round. Bottom: Schematic block diagram for the experimental implementation of the closed-loop feedback control of the qubit frequency. **b** Main panel: Time trace of the qubit frequencies, i.e., the oscillation frequencies of the Ramsey fringe, with (red) and without (blue) frequency locking showing frequency stabilization to the target of 2 MHz with the frequency feedback. Inset: Histogram of the qubit frequencies showing achievement of frequency uncertainty $\sigma = 65.3$ kHz with closed-loop control. **c** PSD of the noise with (red) and without (blue) frequency feedback. The dashed lines represent a power-law fit, yielding the noise amplitude $A$ of 837 kHz²/Hz (1553 kHz²/Hz) and the exponent $\beta$ of 0.945 (1.176) with (without) the frequency feedback. **d** Coherent Ramsey experiments with feedback control showing a stabilized oscillation frequency of about 1.7 MHz. **e** Comparison of $T_2^*$ measured by Ramsey experiments with (red) and without (blue) frequency feedback. The coherence time is measured by fitting the experimental data to the Gaussian decay (solid curves). **f** Improved quality of coherent Rabi chevron pattern in adaptive frequency control mode.

expected to follow the $\chi_k^2$ distribution with a mean $k$ and standard deviation $\sqrt{2k}$ if the observed data is well fitted to the model. $\log L_{max,s}$ shows the theoretical upper bound of the GST model, and $k$ is the number of independent outcomes of a single circuit[44].

Figure 5d shows a significant degree of non-Markovian noise in the non-adaptive control case indicated by the colored boxes, displaying the values $2\Delta \log L_s$ that are outside of the range in Eq. (2) (with a confidence level of 95%, $17 < 2\Delta \log L_s$). In Fig. 5e, the use of both active and passive techniques significantly reduces the impact of non-Markovian noise, as indicated by the decrease in the total amount of the log-likelihood ratios $2\Delta \log L = \sum_s 2\Delta \log L_s$ from 475.7, 3122.8, 4805.3, 6169.1, and 8445.5 (Fig. 5d) to 470.9, 741, 2295.4, 3386.2, and 4835 (Fig. 5e) at maximum lengths of 1, 2, 4, 8, and 16, respectively.

## Discussion

We note that, as shown in Fig. 5e, the violated $2\Delta \log L_s$ that appear differently for each circuit, especially where the Gx germ is used at the length of 16, may indicate temporally inhomogeneous and stochastic errors, which could not be addressed by either technique, such as slow fluctuations in the readout point. Although the magnitude of the goodness-of-fit quantified by GST does not correspond to the actual amplitude of non-Markovian noise, the model violations indicate that the system is unlikely to adhere to a Markov process with high probability. These non-Markovian properties were evident from the noise

spectroscopy exhibiting sub-diffusive behavior attributed to time-correlation as depicted by the nonlinear function in Fig. 3c. In this context, the Bayesian inference employed to reveal the noise characteristics also enabled us to suppress the corresponding noise.

Of the two noise suppression techniques developed in this work, the passive suppression technique by dynamically pulsing SD provides a simple mitigation strategy to minimize the effect of the detector while maintaining high charge sensitivity benefiting from strong sensor-qubit capacitive coupling. Moreover, using SD as a controllable noise source combined with fast noise spectroscopy (see Supplementary Note. 5) may offer a deeper understanding of transduced noise characteristics[45]. The noise source-agnostic active feedback strategy provides a general noise suppression method with an affordable experimental overhead. In the future, a higher sampling rate for noise estimation will enable noise analysis in the wider frequency domain and further decrease the gate infidelity which can be realized for example by optimizing the real-time Bayesian calculation time on the hardware level, minimizing the heating effect that enables minimal waiting time after qubit manipulation, and by reducing the readout time using different spin to charge conversion method such as Pauli spin blockade-based parity measurements[7,46] (see Supplementary Note 6). Parallel with efforts to reduce charge noise source by material development[47–49] and optimizing device fabrication steps[50–52], fast intermittent correction of qubit parameter
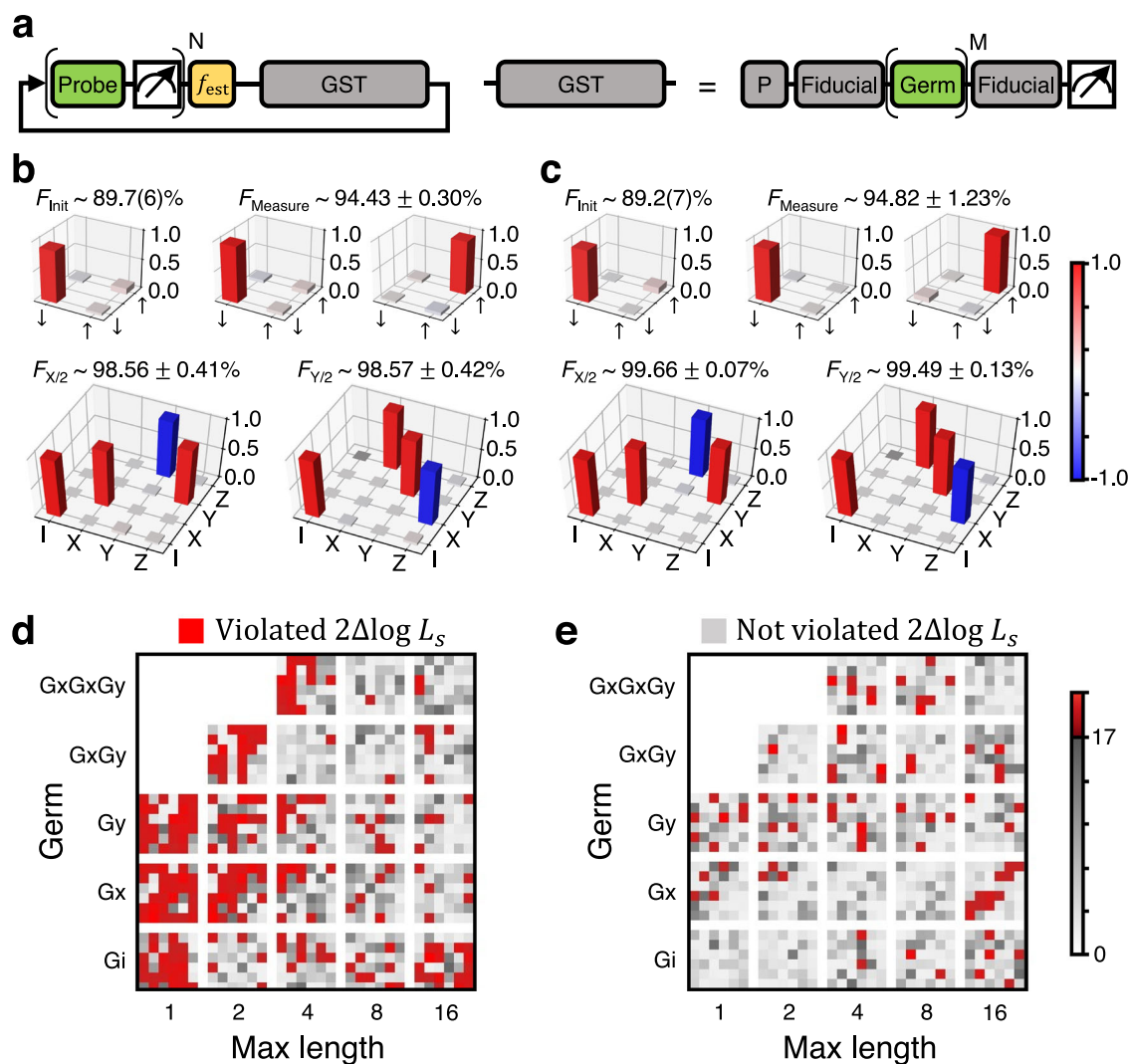
**Fig. 5 | Gate set tomography and model violation. a** A gate set tomography (GST) sequence combined with active frequency feedback. Top row: Density matrices obtained by GST showing fidelity of state preparation and measurement without (**b**) and with (**c**) active and passive noise suppression techniques. Bottom row: Pauli transfer matrices of logic gates without (**b**) and with (**c**) active and passive noise suppression techniques. Error bars represent 95% ($2\sigma$) confidence intervals computed using Monte Carlo bootstrap resampling[4,7]. Model violation plot without (**d**) and with (**e**) active and passive noise suppression. The maximum length is the number of gate operations in a germ circuit. The red marks indicate detections of model violation at a confidence level of more than 95% and the gray boxes indicate statistical fluctuations.

fluctuation[19,53–55] can further enhance the performance of the quantum measurement system.

## Methods

### Device fabrication

Quantum dot qubit devices were fabricated on an undoped $^{28}$Si/SiGe heterostructure featuring a 9 nm quantum well with a residual $^{29}$Si concentration of 0.08%. The quantum well is grown on a strain-relaxed $Si_{0.7}Ge_{0.3}$ substrate and is separated from the surface by a 30 nm $Si_{0.7}Ge_{0.3}$ spacer terminated by an amorphous Si-rich layer[48]. After defining the active region and alignment markers by reactive ion etching, an ohmic region was created via ion implantation with phosphorus, and the device was subsequently annealed to activate the implanted carriers. To suppress leakage, a 30 nm layer of $Al_2O_3$ is deposited on the substrate using Atomic Layer Deposition (ALD). Metal gates and additional oxide layers are formed through repetitive electron-beam lithography steps, metal evaporations of 5 nm Ti / 30 nm Pd using an e-beam evaporator, and ALD steps. The patterned micromagnet on top of the final $Al_2O_3$ layer was deposited using an e-beam evaporator.

### Bayesian inference

Qubit frequency estimation was conducted using Bayes' rule[15,27]. The estimation was based on measurement information $m_k$ obtained from the single-shot outcome of the Ramsey oscillation experiment with a free evolution time $t_k = k \times 40$ ns. The posterior distribution was approximated using an oscillatory likelihood function,

$$P(f|m_N, m_{N-1}, \ldots m_1) = P_0(f) \prod_{k=1}^{N} \frac{1}{2}[1 + r_k(\alpha + \beta \cos(2\pi f t_k + \theta))] \quad (1)$$

where we used the repetition number $N = 100$ per one frequency estimation. $r_k = 1 (-1)$ for $m_k = \downarrow (\uparrow)$, $\theta$ denotes the initial phase of off-resonant Ramsey oscillation, and $\alpha (\beta)$ is determined by errors in the axis of rotation on the Bloch sphere (oscillation visibility). For initial frequency estimation, $P_0(f)$ was initialized as a uniform distribution reflecting a lack of prior knowledge and multiplied by the likelihood functions with $r_1$ and $t_1$. After the Nth single-shot measurement and update, the most probable $f_{est}$ was determined from $P(f|m_{100}, m_{99}, \ldots m_1)$. However, whenever the previously estimated value of $f_{est}$ is available, we set a Gaussian prior distribution $P_0(f)$ with a

mean equal to the previously estimated value having a constant deviation of 50 kHz.

## Gate Set Tomography (GST)

GST characterizes the behavior of quantum gates, the building blocks of quantum circuits, and provides the dataset for analyzing how well these gates perform their intended operations. For the specific purpose of identifying errors, GST uses structured and periodic sequences. Two fiducials {null, X/2, Y/2, X/2∘X/2, X/2∘X/2∘X/2, Y/2∘Y/2∘Y/2} constitute a small 6 × 6 circuit structure as shown in Fig. 5d, e. The germs {I, X/2, Y/2, X/2∘Y/2, X/2∘X/2∘Y/2} between the two fiducials, as shown in Fig. 5a, amplify errors by repeating gate operations. The datasets are generated by recording the results for each specific circuit.

## Fidelity for gate set tomography

In GST, a quantum state is typically described by a $d \times d$ density matrix $\rho$ on a $d$-dimensional Hilbert space, while superoperators $M$ are represented as $d^2 \times d^2$ matrices in the Hilbert-Schmidt space where a basis is chosen as the four Pauli matrices {$\sigma_I$, $\sigma_X$, $\sigma_Y$, $\sigma_Z$} for $d = 2$. GST estimates of $\rho_{exp}$ and $M_{exp}$ involve using a maximum-likelihood estimator to compute completely positive and trace-preserving (CPTP) matrices, given raw measurement outcomes for each circuit in the dataset. Initialization and measurement fidelities can be calculated by evaluating the closeness between the ideal quantum state $\rho_{ideal}$ and the measured state $\rho_{exp}$, $F_{I,M} = (\mathrm{Tr}\sqrt{\sqrt{\rho_{ideal}}\rho_{exp}\sqrt{\rho_{ideal}}})^2$. Furthermore, by comparing the measured Pauli transfer matrix $M_{exp}$ with the ideal $M_{ideal}$, the gate fidelity is given by $F_{gate} = (\mathrm{Tr}(M_{exp}^{-1}M_{ideal}) + d)/[d(d+1)]$.

Error analysis was conducted using Monte Carlo bootstrap resampling. We assume sampling distributions for the CPTP matrices obtained from the GST estimates, and then random samples were repeatedly drawn from these distributions. We generate 1000 datasets to analyze, producing point estimates for each, and use their deviation to define a confidence region.

## Data availability

The data that support the findings of this study are available from the corresponding author upon request.

## References

1. Zwanenburg, F. A. et al. Silicon quantum electronics. *Rev. Mod. Phys.* **85**, 961–1019 (2013).
2. Chatterjee, A. et al. Semiconductor qubits in practice. *Nat. Rev. Phys.* **3**, 157–177 (2021).
3. Burkard, G., Ladd, T. D., Pan, A., Nichol, J. M. & Petta, J. R. Semiconductor spin qubits. *Rev. Mod. Phys.* **95**, 025003 (2023).
4. Takeda, K. et al. Quantum tomography of an entangled three-qubit state in silicon. *Nat. Nanotechnol.* **16**, 965–969 (2021).
5. Hendrickx, N. W. et al. A four-qubit germanium quantum processor. *Nature* **591**, 580–585 (2021).
6. Mądzik, M. T. et al. Precision tomography of a three-qubit donor quantum processor in silicon. *Nature* **601**, 348–353 (2022).
7. Philips, S. G. J. et al. Universal control of a six-qubit quantum processor in silicon. *Nature* **609**, 919–924 (2022).
8. Yoneda, J. et al. A quantum-dot spin qubit with coherence limited by charge noise and fidelity higher than 99.9%. *Nat. Nanotechnol.* **13**, 102–106 (2018).
9. Yang, C. H. et al. Silicon qubit fidelities approaching incoherent noise limits via pulse engineering. *Nat. Electron.* **2**, 151–158 (2019).
10. Noiri, A. et al. Fast universal quantum gate above the fault-tolerance threshold in silicon. *Nature* **601**, 338–342 (2022).
11. Xue, X. et al. Quantum logic with spin qubits crossing the surface code threshold. *Nature* **601**, 343–347 (2022).
12. Takeda, K., Noiri, A., Nakajima, T., Kobayashi, T. & Tarucha, S. Quantum error correction with silicon spin qubits. *Nature* **608**, 682–686 (2022).
13. Zajac, D. M., Hazard, T. M., Mi, X., Nielsen, E. & Petta, J. R. Scalable gate architecture for a one-dimensional array of semiconductor spin Qubits. *Phys. Rev. Appl.* **6**, 054013 (2016).
14. Borsoi, F. et al. Shared control of a 16 semiconductor quantum dot crossbar array. *Nat. Nanotechnol.* **19**, 21–27 (2024).
15. Shulman, M. D. et al. Suppressing qubit dephasing using real-time Hamiltonian estimation. *Nat. Commun.* **5**, 5156 (2014).
16. Nakajima, T. et al. Coherence of a driven electron spin qubit actively decoupled from Quasistatic Noise. *Phys. Rev. X* **10**, 011060 (2020).
17. Kim, J. et al. Approaching ideal visibility in singlet-triplet qubit operations using energy-selective tunneling-based hamiltonian estimation. *Phys. Rev. Lett.* **129**, 040501 (2022).
18. Yun, J. et al. Probing two-qubit capacitive interactions beyond bilinear regime using dual Hamiltonian parameter estimations. *npj Quantum Inf.* **9**, 1–7 (2023).
19. Berritta, F. et al. Real-time two-axis control of a spin qubit. *Nat. Commun.* **15**, 1676 (2024).
20. Vijay, R. et al. Stabilizing Rabi oscillations in a superconducting qubit using quantum feedback. *Nature* **490**, 77–80 (2012).
21. Vepsäläinen, A. et al. Improving qubit coherence using closed-loop feedback. *Nat. Commun.* **13**, 1932 (2022).
22. Acosta, V. M. et al. Dynamic stabilization of the optical resonances of single nitrogen-vacancy centers in diamond. *Phys. Rev. Lett.* **108**, 206401 (2012).
23. Johnson, K. G. et al. Active stabilization of ion trap radiofrequency potentials. *Rev. Sci. Instrum.* **87**, 053110 (2016).
24. Dumoulin Stuyck, N. et al. Silicon spin qubit noise characterization using real-time feedback protocols and wavelet analysis. *Appl. Phys. Lett.* **124**, 114003 (2024).
25. Pioro-Ladrière, M. et al. Electrically driven single-electron spin resonance in a slanting Zeeman field. *Nat. Phys.* **4**, 776–779 (2008).
26. Yoneda, J. et al. Robust micromagnet design for fast electrical manipulations of single spins in quantum dots. *Appl. Phys. Express* **8**, 084401 (2015).
27. Sergeevich, A., Chandran, A., Combes, J., Bartlett, S. D. & Wiseman, H. M. Characterization of a qubit Hamiltonian using adaptive measurements in a fixed basis. *Phys. Rev. A* **84**, 052315 (2011).
28. Zajac, D. M., Hazard, T. M., Mi, X., Wang, K. & Petta, J. R. A reconfigurable gate architecture for Si/SiGe quantum dots. *Appl. Phys. Lett.* **106**, 223507 (2015).
29. Elzerman, J. M. et al. Single-shot read-out of an individual electron spin in a quantum dot. *Nature* **430**, 431–435 (2004).
30. Schoelkopf, R. J., Wahlgren, P., Kozhevnikov, A. A., Delsing, P. & Prober, D. E. The Radio-Frequency Single-Electron Transistor (RF-SET): a fast and ultrasensitive electrometer. *Science* **280**, 1238–1242 (1998).
31. Lu, W., Ji, Z., Pfeiffer, L., West, K. W. & Rimberg, A. J. Real-time detection of electron tunnelling in a quantum dot. *Nature* **423**, 422–425 (2003).
32. Reilly, D. J., Marcus, C. M., Hanson, M. P. & Gossard, A. C. Fast single-charge sensing with a rf quantum point contact. *Appl. Phys. Lett.* **91**, 162101 (2007).
33. Hell, M., Wegewijs, M. R. & DiVincenzo, D. P. Coherent backaction of quantum dot detectors: Qubit isospin precession. *Phys. Rev. B* **89**, 195405 (2014).
34. Hell, M., Wegewijs, M. R. & DiVincenzo, D. P. Qubit quantum-dot sensors: noise cancellation by coherent backaction, initial slips, and elliptical precession. *Phys. Rev. B* **93**, 045418 (2016).
35. Bluhm, H. et al. Dephasing time of GaAs electron-spin qubits coupled to a nuclear bath exceeding 200 μs. *Nat. Phys.* **7**, 109–113 (2011).

36. Hatridge, M. et al. Quantum back-action of an individual variable-strength measurement. *Science* **339**, 178–181 (2013).

37. Undseth, B. et al. Hotter is easier: unexpected temperature dependence of Spin Qubit frequencies. *Phys. Rev. X* **13**, 041015 (2023).

38. Delbecq, M. R. et al. Quantum dephasing in a gated GaAs triple quantum dot due to nonergodic noise. *Phys. Rev. Lett.* **116**, 046802 (2016).

39. Ithier, G. et al. Decoherence in a superconducting quantum bit circuit. *Phys. Rev. B* **72**, 134519 (2005).

40. Cywiński, Ł., Lutchyn, R. M., Nave, C. P. & Das Sarma, S. How to enhance dephasing time in superconducting qubits. *Phys. Rev. B* **77**, 174509 (2008).

41. Yoneda, J. et al. Noise-correlation spectrum for a pair of spin qubits in silicon. *Nat. Phys.* **19**, 1793–1798 (2023).

42. Rojas-Arias, J. S. et al. Spatial noise correlations beyond nearest neighbors in 28Si/Si-Ge spin qubits. *Phys. Rev. Appl.* **20**, 054024 (2023).

43. Blume-Kohout, R. et al. Demonstration of qubit operations below a rigorous fault tolerance threshold with gate set tomography. *Nat. Commun.* **8**, 14485 (2017).

44. Nielsen, E. et al. Gate set tomography. *Quantum* **5**, 557 (2021).

45. Clément, N., Nishiguchi, K., Fujiwara, A. & Vuillaume, D. One-by-one trap activation in silicon nanowire transistors. *Nat. Commun.* **1**, 92 (2010).

46. Seedhouse, A. E. et al. Pauli Blockade in Silicon Quantum Dots with Spin-Orbit Control. *PRX Quantum* **2**, 010303 (2021).

47. de Leon, N. P. et al. Materials challenges and opportunities for quantum computing hardware. *Science* **372**, eabb2823 (2021).

48. Degli Esposti, D. et al. Wafer-scale low-disorder 2DEG in 28Si/SiGe without an epitaxial Si cap. *Appl. Phys. Lett.* **120**, 184003 (2022).

49. Paquelet Wuetz, B. et al. Reducing charge noise in quantum dots by using thin silicon quantum wells. *Nat. Commun.* **14**, 1385 (2023).

50. Connors, E. J., Nelson, J., Qiao, H., Edge, L. F. & Nichol, J. M. Low-frequency charge noise in Si/SiGe quantum dots. *Phys. Rev. B* **100**, 165305 (2019).

51. Eenink, H. G. J. et al. Tunable coupling and isolation of single electrons in silicon metal-oxide-semiconductor quantum dots. *Nano Lett.* **19**, 8653–8657 (2019).

52. Dodson, J. P. et al. Fabrication process and failure analysis for robust quantum dots in silicon. *Nanotechnology* **31**, 505001 (2020).

53. Bonato, C. & Berry, D. W. Adaptive tracking of a time-varying field with a quantum sensor. *Phys. Rev. A* **95**, 052348 (2017).

54. Gutierrez-Rubio, A., Stano, P. & Loss, D. Optimal frequency estimation and its application to quantum dots. Preprint at https://doi.org/10.48550/arXiv.2004.12049 (2021).

55. Benestad, J., Krzywda, J., van Nieuwenburg, E. & Danon, J. Efficient adaptive Bayesian estimation of a slowly fluctuating Overhauser field gradient. *SciPost Phys.* **17**, 014 (2024).

## Acknowledgements

## Author contributions

J.P. fabricated the device with the help of B.K., H.S., J.Y., and Y.S. J.P. and H.J. performed the measurements and configured the measurement software. L.E.A.S., D.D.E., and G.S. synthesized and provided the 28Si/SiGe heterostructure. All authors contributed to the preparation of the manuscript. D.K. supervised the project.

## Competing interests

The authors declare no competing interests.

## Additional information

**Supplementary information** The online version contains supplementary material available at https://doi.org/10.1038/s41467-024-55338-z.

**Correspondence** and requests for materials should be addressed to Dohun Kim.

**Peer review information** *Nature Communications* thanks Jan Krzywda, Chih-Hwan Yang, and the other, anonymous, reviewer for their contribution to the peer review of this work. A peer review file is available.

**Reprints and permissions information** is available at http://www.nature.com/reprints

**Publisher's note** Springer Nature remains neutral with regard to jurisdictional claims in published maps and institutional affiliations.